

Journal Pre-proofs

Extended Properties of Magnetic Spins of Zinc Ferrite Nanoparticles in the THz Frequency Range

Mohamed Hassan Abdellatif, Martin Etter, Petra Fromme, Marco Salerno

PII: S0304-8853(20)32541-5
DOI: <https://doi.org/10.1016/j.jmmm.2020.167574>
Reference: MAGMA 167574

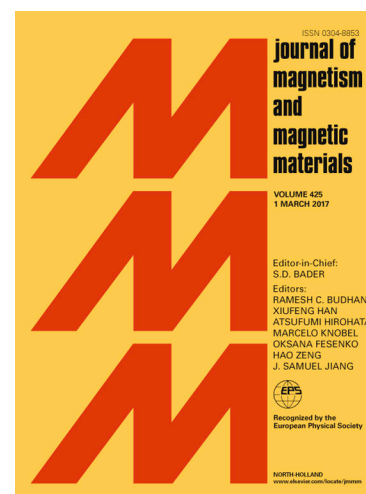
To appear in: *Journal of Magnetism and Magnetic Materials*

Received Date: 1 July 2020
Revised Date: 22 October 2020
Accepted Date: 12 November 2020

Please cite this article as: M. Hassan Abdellatif, M. Etter, P. Fromme, M. Salerno, Extended Properties of Magnetic Spins of Zinc Ferrite Nanoparticles in the THz Frequency Range, *Journal of Magnetism and Magnetic Materials* (2020), doi: <https://doi.org/10.1016/j.jmmm.2020.167574>

This is a PDF file of an article that has undergone enhancements after acceptance, such as the addition of a cover page and metadata, and formatting for readability, but it is not yet the definitive version of record. This version will undergo additional copyediting, typesetting and review before it is published in its final form, but we are providing this version to give early visibility of the article. Please note that, during the production process, errors may be discovered which could affect the content, and all legal disclaimers that apply to the journal pertain.

© 2020 Published by Elsevier B.V.



"Your paper your way" format

Extended Properties of Magnetic Spins of Zinc Ferrite Nanoparticles in the THz Frequency Range

Mohamed Hassan Abdellatif¹, Martin Etter², Petra Fromme^{3,4} and Marco Salerno^{5,6*}

¹ Center for Free Electron Laser Science, Deutsches Elektronen Synchrotron, Notkestrasse 85, 22607 Hamburg Germany

² Deutsches Elektronen Synchrotron, FS-PETRA-D, P02.1, Notkestr. 85, 22607 Hamburg, Germany

³ Biodesign Center for Applied Structural Discovery, Arizona State University, Tempe, AZ 85287-5001, USA

⁴ School of Molecular Sciences, Arizona State University, Tempe, AZ 85287-1604, USA

⁵ Materials Characterization Facility, Istituto Italiano di Tecnologia, via Morego 30, 16163 Genova, Italy

⁶ The Ronin Institute, Montclair, NJ, 07043, USA

*corresponding author: marco.salerno@iit.it

Abstract (182 words)

We fabricated nanoparticles of Zn ferrite of the chemical formula ZnFe_2O_4 using the auto-combustion technique, and investigated their magnetic spin distribution and frequency response to optical excitation. Optical absorption and magnetic characterization of the nanoparticles were carried out in the UV-Vis and IR range, and extended on the low frequency side down to the THz domain. The nanoparticles were also characterized by X-ray diffraction and by magnetic force microscopy. The optical dielectric constant was calculated in both the UV-Vis and the THz domain. The optical bandgap, the dispersion energy and the oscillator strength of the nanoparticles were calculated from the optical data based on the single oscillator model. We measured the optical absorption, transmission and reflection spectra in the wavelength range from 200 to 800 nm, and calculated the refractive index, absorption and extinction coefficient. The optical band gap was found to be 1.14 eV and the oscillating energy of the dipole was determined to be 6.94 eV. The study shows that the coordination number of a metal complex and the symmetrical arrangement play an important role in determining the nanoparticle properties.

Keywords: Zinc ferrite; nanoparticles; magnetic properties; magnetic force microscopy; dielectric constant; Wemple-DiDomenico model

1. Introduction

Coordination number and lattice symmetry play an important role in determining the material properties of metal complexes. Actually, cation distribution, symmetry and metal coordination are basically referring to the same concept expressed in different words, in which the properties of the material are determined by the metal cation location in the studied crystal^{1–7}. Spinel ferrites may represent a simple model to investigate the effect of metal coordination on the magnetic properties of these materials, at excitation frequencies between optical spectrum and THz. In recent years THz spectroscopy became a hot topic based on its possible use in several daily life applications⁸, especially in the area of wideband wireless communication^{9,10}. Ferrites in particular are playing an increasing role in THz technology alternative to their magnetic interactions, which result in applications such as THz phase-shifters, isolators, and couplers^{11–13}. The fact that for most magnetic materials the magnetism vanishes above THz frequencies, helped in designing metamaterials with specific periodicity that simulates artificial magnetism^{14,15}. Some progress has also been achieved in imaging applications for biological samples, using THz radiation^{16,17}. The THz spectral range extends in frequency from the lower limit of 0.3 THz up to 10 THz, following Lee's definition¹⁸. Several options exist for generation of frequencies in that range, among which are the photo-mixer technique¹⁹ and the use of specialized THz beam lines at synchrotron light sources²⁰. On the other hand, the THz time-domain spectroscopy (THz–TDS) is a well-established method to determine the complex refractive index for materials in the long-wavelength region, by comparing the THz broadband pulse passing through the sample with that one transmitted in the air as a reference signal, and applying Fourier transform that yields a transfer function. Actually, THz–TDS is the most common technique to measure the amplitude and phase responses to electromagnetic excitation in the time domain, an approach whose basics concepts can be found in Ref.²². Telecommunications are expanding over a wide range of frequencies in the THz range, which opens a demand to characterize ferroelectrics as guiding material for these wavelengths. Therefore, evaluation of the dielectric properties of materials at sub-THz and THz frequencies has become important, due to substantial industrial relevance. By applying THz-TDS spectroscopy, one can determine the real and imaginary part of the dielectric constant with usually higher accuracy than with indirect optical techniques^{23–25}.

Ferrites have a spinel structure of the general formula of MFe_2O_4 , where M is a divalent metal ion, which occupies one of the interstitial sites according to ion valence and size such as Cu and Zn²⁶. Ferrites have found so far several technological applications

thanks to their properties, such as in gas sensing ²⁷, in drug delivery ²⁸, as photocatalyst ²⁹ and as humidity sensors ^{30,31}. There Ferrite thin films are widely used in magnetic recording heads, owing to their excellent soft magnetic properties, such as high permeability and low coercivity ^{32,33}. Ferrite nanoparticles (NPs) have found a wide range of applications, such as in micro-inductor, in micro-transformers, and in GHz frequency applications ^{34,35}. The spin distribution and wideband THz absorption are hot topics in the characterization of magnetic NPs.

In this work, we investigated the optical properties of the ferrite NPs as magnetic materials in the UV-Vis and IR domain, extending the latter down to THz frequencies, with particular attention on their dependence on the metal coordination. We have characterized the magnetic spins, measured the optical transmission and absorption, and extracted the dielectric constant, oscillator strength, and dispersion energy and absorption coefficient.

2. Methods

All chemicals were purchased from Sigma-Aldrich (Germany), and used as received. The ferrite nano-powder was prepared using the sol-gel auto-combustion method. We started from a 1:2 molar ratio of zinc nitrate ($\text{Zn}(\text{NO}_3)_2$, 1.894 g) and ferric nitrate ($\text{Fe}(\text{NO}_3)_3 \cdot 9\text{H}_2\text{O}$, 8.08 g). The compounds were mixed with a solution of 150 mL water and 5.764 g citric acid ($\text{C}_6\text{H}_8\text{O}_7$). Once a clear solution was formed, with pH in the range of 2-3, we started adding 70 wt% ammonia (NH_3) aqueous solution in dropwise manner, while controlling the resulting pH, until it reached 7.0. The mixture was put on a hot-plate set to 150°C under continuous stirring, such that slow evaporation took place until a gel was formed, typically after 40-60 min. Then, the stirring was switched off while the temperature was still kept at 150°C, which led to strong auto-combustion of the gel, a process in which the NPs started forming from the bottom of the beaker like a tree. More details about the preparation conditions can be found in Ref. ³⁶.

The sample was first characterized by powder X-ray diffraction (PXRD) at the powder diffraction and total scattering beamline P02.1 (PETRA III at DESY, Hamburg, Germany), with wavelength of 0.20722 Å.

Then, optical absorbance spectroscopy was carried out on an aqueous suspension of the powder (typically 1 wt%), first with an UV-Vis spectrometer 2700 (Shimadzu, Japan), then using a THz-TDS spectrometer (Tera OSCAT, Menlo, USA) in the low frequency range, down to 5 THz. The commercial setup consisted of a fiber-based laser system centered at 1560 nm wavelength, which was used to excite the charge carriers in a photo-conductive

antenna. The THz detector was gated with the time delayed laser pulse, which was guided and focused using a pair of off-axis parabolic mirrors. A scheme of the setup is presented in Fig.S1. The extraction of the sample optical parameters was done using a previously described procedure^{37–39}, according to the equations presented later on in the text (Results and Discussion). The measurements were carried out on a 1.5 cm diameter disc pellet, with an optimized thickness of 3 mm, obtained from the powder under compression in a steel mold with an equivalent weight for of up to ~1.5 Tonn.

Finally, the magnetic spins in clustered NPs were characterized by magnetic force microscopy (MFM), with an instrument XE-100 (Park Systems, Korea), using MFMV probes (Bruker, USA). To this goal, we suspended the NPs in a 5% wt solution in Anisole, and spin coated it onto atomically flat silicon wafer substrate, at 2000 rpm for 1 min. According to former calibration curve of film thickness vs rotation speed obtained by measuring step-height with the atomic force microscope across scratches handmade in the films, the expected film thickness in these conditions was ~50 nm. This was enough to keep the NPs adhered to the substrate, during subsequent MFM scanning, yet without burying them deep into the film, which would hinder their magnetic response.

3. Results and Discussion

Fig.1 shows the 1D PXRD pattern of the manufactured powder compound, which appears to be the single phase of a cubic spinel crystal ferrite structure (matching to the JCPDS Card No. 89-7412) with space group $Fd-3m$. No other peaks corresponding to different phases or impurities are observed.

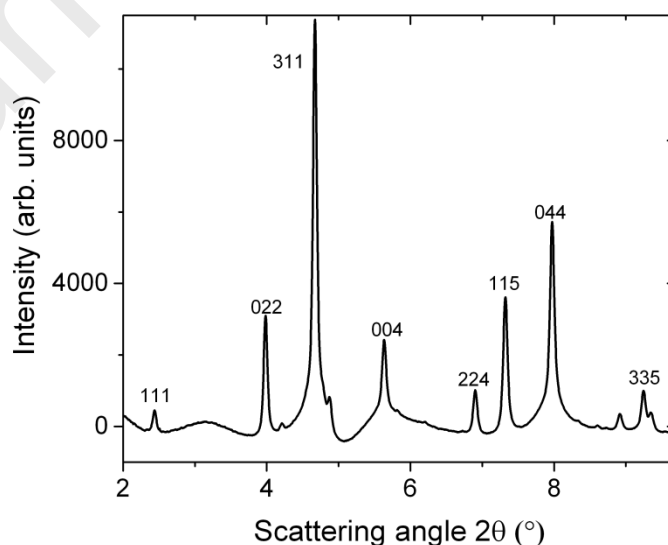


Fig. 1: PXRD pattern of Zn-ferrite NPs. The peaks fit to the cubic spinel structure of ZnFe_2O_4 .

In Fig.2, the typical result of a measurement carried out with THz spectroscopy is illustrated. Actually, it is the time delay Δt between the signal passing through the sample and the reference signal that allows one to estimate the refractive index n of the material, according to the following formula:

$$\Delta t = (n - 1) \frac{d}{c} \quad (1)$$

where d is the material thickness and c is the speed of light.

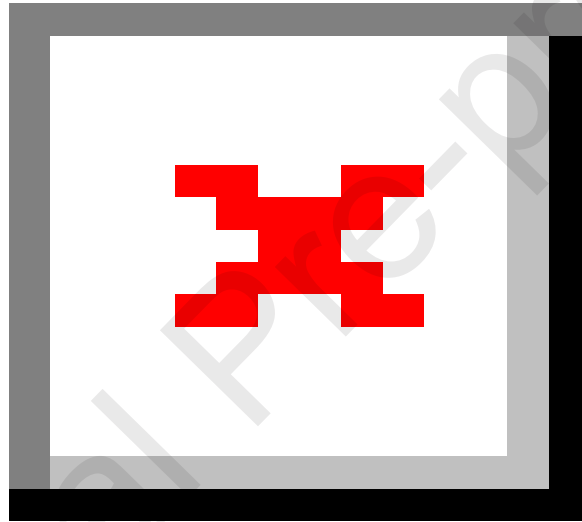


Fig. 2: THz spectroscopy measurement. a) THz reference and signal after passing through the Zn-ferrite sample, showing a delay of 15.177 ps; b) absorption signal in the frequency domain; c) imaginary part of the dielectric modulus.

A sketch of the setup is shown in Fig.S1. The THz reference signal approached the background noise level at 2.5 THz. During the TDS measurement, the THz pulses travel back and forth inside the sample in a Fabry-Perot manner, which results in multiple copies of the main pulse in a thin sample, appearing in the recorded THz signal. Therefore, while

on the one hand use of a thicker sample was favorable to isolate the THz pulse from its reflection, on the other hand the sample could not be too thick, since the length of the time window in TDS THz was limited. After some trials, we found a good compromise for $d \approx 3$ mm.

Fig.2a shows the raw data, which is the time domain profile of the sample response with respect to the reference signal. The traces are shifted in ordinate direction with respect to each other, for clarity. The recorded time delay Δt (see eq.1) was found to be 15.2 ps. The frequency domain spectra was obtained from the time domain profile, using fast Fourier transform, and the resulting data is shown in Fig.2b.

It should be noted that we assume a flat material surface with a homogeneous structure, and the spikes that can be seen in the spectrum of Fig.2b, mainly on the left side of the peak, are due to deviation from this assumption^{39–41}. There appear to be also absorption peaks around 0.7 and 2 THz, which can be attributed to the frequency of precession of the magnetic spin^{42–44}. Indeed, it is known that THz pulses are helpful in controlling the spin response of magnetic materials, which can be a new door into controlling magneto electric structures^{45,46}. The physical base for understanding this effect is described hereafter. Considering a magnetic material, some lattice distortion will force the spins to be canted, and the result will be appearance of a precession motion around the c -axis, with extinction oscillation wave of frequency $\omega_r = \gamma H_0$, where γ is the gyromagnetic ratio and H_0 is the external applied magnetic field. If a similar frequency wave hits the sample, it will be in resonance and will be then highly absorbed. In general, the electronic spins are usually in the microwave region, close to THz radiation. However, in materials similar to our ferrite, the magnetic interactions arise from the interaction between the magnetic sublattices, the tilted geometry, and the anisotropy in the sublattices^{47–50}. Considering the different responses of the magnetic sublattices due to their spontaneous magnetization, if the exchange interaction field is high enough,^{2,51} the precession resonance frequency will reach sub-THz scale. Since the magnetic sublattices differ in their magnetic moment due to different cation occupancy, then the exchange interaction field is proportional to their magnetic moment through a constant, and it follows that the above precession resonant frequency can be written as:

$$\omega_r = \gamma \sqrt{H_a(H_a + 2H_{ex})} = \gamma H_{eff}, \quad (2)$$

where H_{eff} is the effective magnetic field, resulting from the combination of the anisotropy field H_a and of the exchange interaction H_{ex} . This canting effect will be higher if the Fe ions

hybridize with nearby cations in the octahedral or tetrahedral site which results in a non-zero orbital angular momentum. When the THz mm-long wave interacts with the zero-field ferromagnetic resonance, the magnetic field component of the THz pulse tilts the spontaneous magnetization far from the easy axis, due to gyromagnetic effect. The result is that the whole bulk magnetization precesses around the axis at the particular absorption frequency. Although the resonance in Fig.2b looks weak, the magnetic response in THz frequencies domain is not common and is therefore considerable. Eventually, many applications could result based on these phenomena, such as THz wave isolator, rotator or wave absorber as well as reducing interference problems ^{52,53}.

In Fig.2c, the imaginary part M'' of the complex dielectric modulus has also been plotted ⁵⁴, which has been calculated after the following formula:

$$M'' = \frac{\varepsilon''}{\varepsilon'^2 + \varepsilon''^2} \quad (3)$$

Indeed it appears that M'' shows two peaks at frequency values close to those suggested in Fig.2b, and more exactly at 0.73 and 2.02 THz.

The complex optical constants of our sample were calculated indirectly by measuring the variation of the THz electric field passing through the sample, in the domain of angular frequency ω , as represented in Fig.2. Thus, the complex refractive index of the sample material $\hat{n}(\omega) = n(\omega) - ik(\omega)$ can be obtained, where $n(\omega)$ is the refractive index and $k(\omega)$ is the extinction coefficient, and this can be in turn correlated with the also complex dielectric constant $\hat{\varepsilon}(\omega) = \varepsilon'(\omega) + \varepsilon''(\omega)$, where it is:

$$\varepsilon' = n^2 - k^2, \varepsilon'' = 2nk \quad (4)$$

In Fig.3a, n and k are plotted versus the incident angular frequency, and a similar plot is used to show ε' and ε'' in Fig.3b.

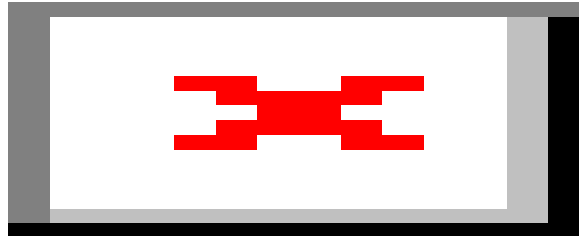


Fig. 3: Spectra of optical properties resulting from the THz measurement: a) refractive index and extinction coefficient, b) real and imaginary part of the dielectric constant.

Fig.4a shows the optical transmittance and reflectance spectra measured in the UV-Vis range, and the dependence of the absorption coefficient α on the incident photon wavelength, as calculated from the measured data using the following equation:

$$\alpha = \frac{1}{d} \ln \left[\frac{(1-R)^2}{2T} + \sqrt{\frac{(1-R)^4}{4T^2} + R^2} \right] \quad (5)$$

where d is the film thickness. The transmittance appears to increase with increasing wavelength, reaching the highest value in the IR region, while the reflectance presents a small peak at ~ 740 nm wavelength, which is ascribed to the Q-band and corresponds to an electronic transition $a_{1u} \rightarrow e_g$.⁵⁵

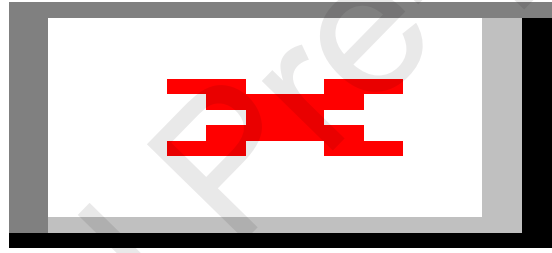


Fig. 4: UV-Vis spectroscopy measurement: a) transmission, reflection and absorption of the Zn-ferrite NPs; b) αE plot versus E , with the respective best fit, according to the theoretical Tauc's relation.

The importance of α is that this coefficient describes the behavior of the light intensity transmitted after the light intensity incident at a given wavelength. This defines the reciprocal thickness over which the light intensity falls to a fraction of $1/e$ with respect to its initial value, due to optical coupling with the electric dipoles of the medium⁵⁶. The type of the electronic and optical transition in ferrite can be evaluated from the dependence of α on the photon energy, using Tauc's equation⁵⁷:

$$\alpha E = p(E - E_g)^m, \quad (6)$$

where p is a constant, $E=h\nu$ is the energy of the photon, E_g is the optical band gap, and m is an exponent determining the type of transition, which is $m=0.5$ for direct allowed, $m=2$ for indirectly allowed, $m=3/2$ for directly forbidden, and $m=2/3$ for the indirect forbidden transition. From Fig.4b one can see that the best fit of the experimental data with eq.6 is obtained for $m=1.5$, which indicates a direct forbidden electronic transition for the fabricated ferrite.

Extrapolating the red line of the fit in Fig.4b, allows one to find the optical band gap value, which turns out to be 1.146 eV. However, this value cannot be taken as a characteristic property of the pristine ferrite material, due to quantum size effect, as quantum effects play a dominant role in determining material parameters^{58–63}.

Ferrite is considered to be a dielectric material, in which the conduction mechanism depends mainly on the polarizability of the electric dipoles, which in turn affects its crystal field and finally its light coupling. The dependence of refractive index n and extinction coefficient k on the incident light energy, has been calculated according to the following expressions:

$$k = \frac{\alpha\lambda}{4\pi}, \quad n = \frac{1+R}{1-R} + \sqrt{\frac{4R}{(1-R)^2} - k^2}, \quad (7)$$

and the resulting spectra are presented in Fig.5a. At the same time, the real and imaginary part of the corresponding dielectric constant, as calculated according to eq.4, have been plotted in Fig.5b.

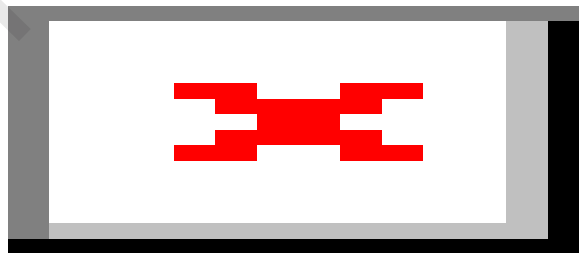


Fig. 5: Spectra of optical properties resulting from the UV-Vis measurement: a) real and imaginary part of the dielectric constant; b) refractive index and extinction coefficient.

In general, n is associated with the dispersion part of the medium, while k is associated with the dissipation rate of the wave in the medium. The peaks appearing in the n and k graphs

of Fig.3a and 5a for the THz and the UV-Vis domain, respectively, are associated with the coupling of light with the electric dipoles. Similar information can be obtained from the plots of ϵ' , ϵ'' in Fig.3b and 5b, respectively, since both are associated with the polarizability of the sample due to its interaction with light, which is indirectly associated with the dissipation and dispersive behavior of the dipoles in the ferrite. The behavior of ϵ' , ϵ'' , and their correlated parameters n and k , coupling with photons of energy $E=h\nu$, can be explained using the single oscillator model ^{64,65}, in which the refractive index is associated with the photon energy through the following equation ⁶⁶:

$$n^2 - 1 = \frac{E_d E_o}{E_o^2 - E^2}, \quad (8)$$

where E_o is the energy of the oscillator, $\hbar\omega$ is the energy of the photon and E_d is the dispersion energy. The latter quantity is a measure of the average strength of the interband optical transition, and is described by the empirical formula:

$$E_d = \beta N_c Z_a N_e \quad (9)$$

where N_c is the coordination number of the cation that is nearest neighbor to the anion, Z_a is the chemical valence of the anion, N_e is the effective number of valence electrons per anion, and β is a constant that depends on the structure and type of bond. Thus, the metal coordination and the symmetrical arrangement of its geometry play an important role in defining the optical and magnetic properties of the material. However, the dependence of the optical response of ferrite can be described in a compact way by the complex dielectric constant $\epsilon(\omega) = \epsilon'(\omega) + i\epsilon''(\omega)$, where $\epsilon'(\omega)$ and $\epsilon''(\omega)$ take into account that electronic excitation is possible only for a certain threshold frequency above the lattice vibration, at which point $\epsilon'(\omega) = n^2(\omega)$.

Fig.6 shows the fit of the Wemple-DiDomenico plot model in eq.9 to the high energy part of the $(n^2-1)^{-1}$ term versus E^2 . The best fitting parameters give a dispersive crystal field E_d of ~282.3 eV, and an energy for the oscillating dipoles of ~6.944 eV.

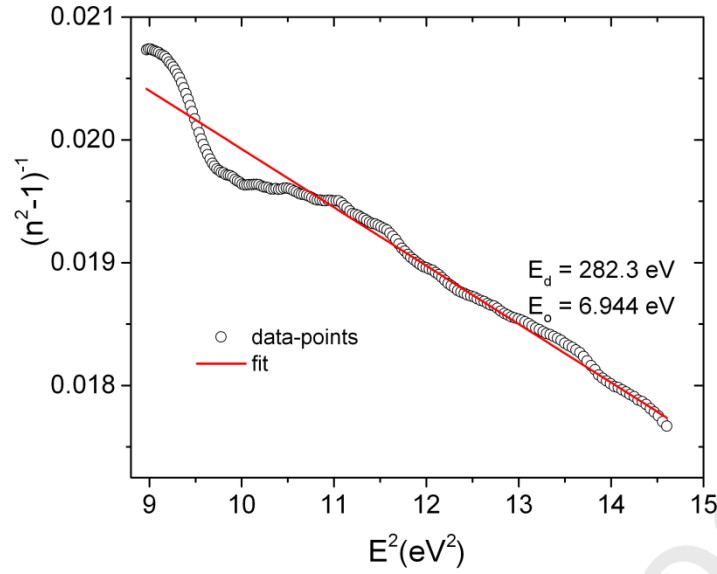


Fig. 6: Experimental plot of the high energy part of the variation of $(n^2-1)^{-1}$ versus E^2 graph, including the fit to the Wemple–DiDomenico single equation model, (fitting parameters are shown in the figure).

One way to characterize the collective interaction of the magnetic behavior of NPs is MFM. By this imaging technique, the magnetic ordering can be characterized and the resulting images can reveal the areas of repulsive and attractive points on the domain wall, whose motion can be modeled as a mass movement in a restoring force field, where the mass is the size of the domain wall and the force is the magnetostatic force field ⁶⁷. Fig.7 shows representative MFM images of different sized Zn-ferrite NPs clusters.

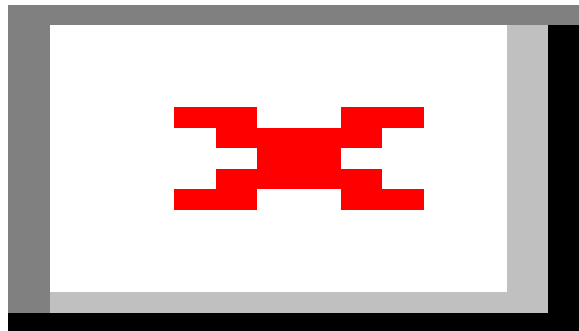


Fig. 7: Representatives MFM images of a typical NP (a,b) and NPs clusters (c,d), showing both the height (a,c) and the cantilever oscillation phase shift (b,d) due to the magnetic force interaction, along with corresponding cross-sections.

The phase shift of the cantilever oscillation is due to the magnetic force arising from magnetic spin ordering, and therefore represents the intensity of this effect qualitatively. The highest magnetic force appears when the spins are parallel or antiparallel to the magnetic tip spins, while the weaker force appears when the different spins are planar parallel to the sample substrate. In particular, MFM cross-sections of height and phase images allow one to better identify the response of the material to the magnetic forces, as compared to the respective top views.

The collective behavior of the magnetic NPs is controlled by the magnetocrystalline anisotropy energy, which is the energy originating from misalignment of the magnetic spins⁴⁸. Due to the small size of primary magnetic NPs, it is energetically unfavorable that more than one magnetic domain exists in the single NPs. As a result, each NP has one single magnetic domain with high magnetic dipole moment. It follows that the long-range dipole interaction is dominant, when it comes to collective behavior of NPs clusters. Fig.8 shows the phase shift of the probe cantilever interacting with the NPs in a number of MFM images such as shown in Fig.7, plotted versus the height of the NPs clusters.

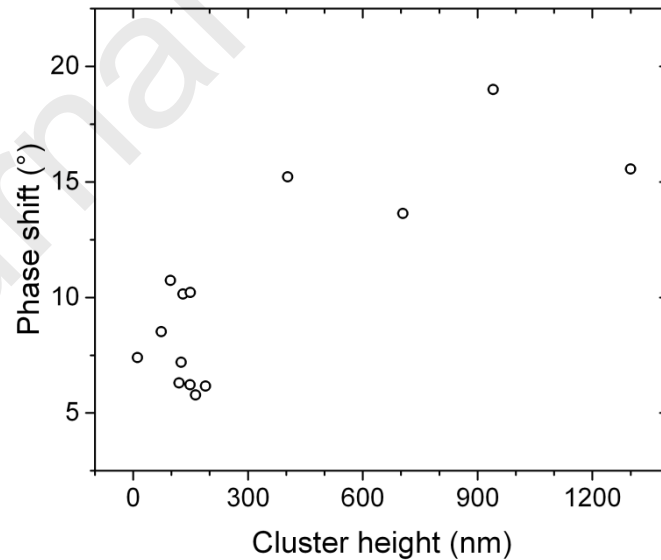


Fig. 8: Plot of phase shift versus height of the magnetic Zn-ferrite NPs clusters as determined by MFM. The magnetic strength of the particles increases with their size in non-linear way.

The zero phase shift corresponds to the condition where very large distance gives rise to negligible interaction. The observed behavior shows that the phase shift is roughly

increasing with increasing sample height, which can be ascribed to the ordering of the spins in the NPs clusters.

4. Conclusion

We fabricated Zinc ferrite NPs with space group $Fd-3m$, and investigated the magnetic and optical properties of the NPs and their clusters. In order to study the magnetic spin behavior and the indirect effect of metal coordination on the physical properties, the samples were characterized in the THz region from 0.2 to 2 THz. In the THz absorption spectra two dips appeared at around 0.7 and 2 THz, which correspond to the resonance frequency of the magnetic spins under the action of THz field, as confirmed by the graph of the complex dielectric modulus. The anisotropic field and the exchange interaction are the two parameters that determine the precession frequency of the magnetic spins, in which the THz absorption takes place. These two parameters are a result of metal coordination, and the symmetry of the Zinc ferrite crystal. Magnetic spins in ferrite materials are highly dependent on the cation distribution in the tetrahedral and octahedral sites, based on the preferences of the cations according to its valance and size. We conclude that metal coordination is the key parameter to understand the optical parameters deduced from the absorption and reflection spectra at 200 to 800 nm. The oscillator strength and the dispersion energy for the investigated NPs were found to be 6.9 eV and 282 eV. There are no parameters that control the behavior of the oscillator other than on the number of cations surrounding the metal and its valence, which determine its type. In conclusion, the symmetry of the crystal structure, the metal arrangement and its distribution on the crystallographic sites are the base parameters that determine the crystal response to the perturbing electromagnetic field.

Acknowledgements

M. H. Abdellatif and Petra Fromme were supported by the European Research Council grant "Frontiers in Attosecond X-ray Science: imaging and spectroscopy (AXSIS)", ERC-2013-SyG 609920.

References:

1. Moustafa, A. M., Farag, I. S. A., Abdellatif, M. H. & Ahmed, M. A. Structural analysis and role of cation distribution on the magnetic properties of single phase Ni-doped copper chromium ferrite. *J. Mater. Sci. Mater. Electron.* (2019). doi:10.1007/s10854-019-02384-9
2. Abdellatif, M. H. *et al.* Effect of Jahn-Teller distortion on the short range magnetic

- order in copper ferrite. *J. Magn. Magn. Mater.* **424**, 402–409 (2017).
3. Salah, L. M., Mabied, A. F. & Abdellatif, M. H. Multiferroic property of $\text{Ca}_{1-x}\text{La}_x\text{Ti}_{1-x}\text{Fe}_x\text{O}_3$ perovskite structure. *J. Magn. Magn. Mater.* **458**, 10–14 (2018).
 4. Abdellatif, M. H., El-Komy, G. M., Azab, A. A. & Moustafa, A. M. Oscillator strength and dispersive energy of dipoles in ferrite thin film. *Mater. Res. Express* **4**, 076410 (2017).
 5. Abdellatif, M. H., El-Komy, G. M. & Azab, A. A. Magnetic Characterization of Rare Earth Doped Spinel Ferrite. *J. Magn. Magn. Mater.* (2017). doi:10.1016/j.jmmm.2017.07.020
 6. Abdellatif, M. H., El-Komy, G. M., Azab, A. A. & Salerno, M. Crystal field distortion of La^{3+} ion-doped Mn-Cr ferrite. *J. Magn. Magn. Mater.* **447**, (2018).
 7. Abdellatif, M. H., Song, J. D., Choi, W. J., Cho, N. K. & Lee, J. I. Quantum dot-like effect in InGaAs/GaAs quantum well. *EPJ Appl. Phys.* **55**, (2011).
 8. Abdul-Munaim, A. M., Ornik, J., Koch, M. & Watson, D. G. Terahertz time domain spectroscopy to detect different oxidation levels of diesel engine oil. *Lubricants* **7**, (2019).
 9. Kleine-Ostmann, T. & Nagatsuma, T. A review on terahertz communications research. *Journal of Infrared, Millimeter, and Terahertz Waves* **32**, 143–171 (2011).
 10. Boss, A. F. N., Migliano, A. C. C. & Wilke, I. Terahertz frequency electrical properties of nickel cobalt ferrites. in *International Conference on Infrared, Millimeter, and Terahertz Waves, IRMMW-THz 2016-Novem*, (IEEE Computer Society, 2016).
 11. Kang, L., Zhao, Q., Zhao, H. & Zhou, J. Magnetic tuning of electrically resonant metamaterial with inclusion of ferrite. *Appl. Phys. Lett.* **93**, (2008).
 12. Bi, K., Zhu, W., Lei, M. & Zhou, J. Magnetically tunable wideband microwave filter using ferrite-based metamaterials. *Appl. Phys. Lett.* **106**, (2015).
 13. Yamaguchi, K., Kurihara, T., Minami, Y., Nakajima, M. & Suemoto, T. Terahertz time-domain observation of spin reorientation in orthoferrite ErFeO_3 through magnetic free induction decay. *Phys. Rev. Lett.* **110**, (2013).
 14. Linden, S. *et al.* Magnetic response of metamaterials at 100 terahertz. *Science* (80-.). **306**, 1351–1353 (2004).
 15. Yen, T. J. *et al.* Terahertz Magnetic Response from Artificial Materials. *Science* (80-.). **303**, 1494–1496 (2004).
 16. Mittleman, D. M. *et al.* Recent advances in terahertz imaging. *Appl. Phys. B Lasers Opt.* **68**, 1085–1094 (1999).
 17. Fischer, B. M., Walther, M. & Jepsen, P. U. Far-infrared vibrational modes of DNA components studied by terahertz time-domain spectroscopy. *Phys. Med. Biol.* **47**, 3807–3814 (2002).
 18. Lee, Y.-S. *Principles of terahertz science and technology*. (Springer, 2009).
 19. McIntosh, K. A. *et al.* Terahertz photomixing with diode lasers in low-temperature-grown GaAs. *Appl. Phys. Lett.* **67**, 3844 (1995).
 20. Spampinati, S. *et al.* Coherent THz Emission Enhanced by Coherent Synchrotron Radiation. 1–8 (2018). doi:10.1038/s41598-018-30125-1
 21. Roy, P., Rouzières, M., Qi, Z. & Chubar, O. The AILES Infrared Beamline on the third generation Synchrotron Radiation Facility SOLEIL. *Infrared Phys. Technol.* **49**, 139–146 (2006).
 22. Bründermann, E., Hübers, H.-W. & Kimmitt, M. F. *Terahertz techniques*.
 23. Buixaderas, E., Nuzhnyy, D., Petzelt, J., Jin, L. & Damjanovic, D. Polar lattice vibrations and phase transition dynamics in $\text{Pb}(\text{Zr}_{1-x}\text{Ti}_x)\text{O}_3$. *Phys. Rev. B - Condens. Matter Mater. Phys.* **84**, (2011).
 24. Chen, L. *et al.* Terahertz Electro-Optic Properties of Two Typical Ferroelectric Materials. **213511**, 411105 (2015).

25. Kwak, M. H. *et al.* Dielectric characteristics of Pb(Zr, Ti)O₃ films on MgO single crystal substrate by terahertz time domain spectroscopy. in *Ferroelectrics* **422**, 19–22 (2011).
26. Gubbala, S., Nathani, H., Koizol, K. & Misra, R. D. K. Magnetic properties of nanocrystalline Ni–Zn, Zn–Mn, and Ni–Mn ferrites synthesized by reverse micelle technique. *Phys. B Condens. Matter* **348**, 317–328 (2004).
27. Ikenaga, N., Ohgaito, Y., Matsushima, H. & Suzuki, T. Preparation of zinc ferrite in the presence of carbon material and its application to hot-gas cleaning. *Fuel* **83**, 661–669 (2004).
28. Shouheng Sun, *,† *et al.* Monodisperse MFe₂O₄ (M = Fe, Co, Mn) Nanoparticles. (2003). doi:10.1021/JA0380852
29. Fan, G., Gu, Z., Yang, L. & Li, F. Nanocrystalline zinc ferrite photocatalysts formed using the colloid mill and hydrothermal technique. *Chem. Eng. J.* **155**, 534–541 (2009).
30. Tsay, C. ., Liu, K. ., Lin, T. . & Lin, I. . Microwave sintering of NiCuZn ferrites and multilayer chip inductors. *J. Magn. Magn. Mater.* **209**, 189–192 (2000).
31. Krishnaveni, T., Kanth, B. R., Raju, V. S. R. & Murthy, S. R. Fabrication of multilayer chip inductors using Ni–Cu–Zn ferrites. *J. Alloys Compd.* **414**, 282–286 (2006).
32. Uemura, T., Yano, T., Matsuda, K. & Yamamoto, M. Analysis of magnetic anisotropy for Co₂Cr_{0.6}Fe_{0.4}Al thin films epitaxially grown on GaAs. *J. Magn. Magn. Mater.* **310**, e696–e698 (2007).
33. Matsuda, H. & Sakakima, H. Studies of magnetization reversals about two kinds of MR curves observed in the spin valve using the (110) magnetite pinning layer. *J. Magn. Magn. Mater.* **324**, 1726–1732 (2012).
34. Swan, R., Ray, A. K. & Hogarth, C. A. Optical absorption in thin tellurium films. *Phys. Status Solidi* **127**, 555–560 (1991).
35. Campbell, D. & Collins, R. A. A study of the interaction between nitrogen dioxide and lead phthalocyanine using electrical conduction and optical absorption. *Thin Solid Films* **295**, 277–282 (1997).
36. Abdellatif, M. H. & Azab, A. A. Fractal Growth of Ferrite Nanoparticles Prepared by Citrate-Gel Auto-Combustion Method. *Silicon* (2018). doi:10.1007/s12633-017-9711-1
37. Wilk, R., Pupez, I., Cernat, R. & Koch, M. Highly accurate THz time-domain spectroscopy of multilayer structures. *IEEE J. Sel. Top. Quantum Electron.* **14**, 392–398 (2008).
38. Scheller, M., Jansen, C. & Koch, M. Analyzing sub-100-μm samples with transmission terahertz time domain spectroscopy. *Opt. Commun.* **282**, 1304–1306 (2009).
39. Pupez, I., Wilk, R. & Koch, M. Highly accurate optical material parameter determination with THz time-domain spectroscopy. *Opt. Express* **15**, 4335 (2007).
40. Duvillaret, L., Garet, F. & Coutaz, J.-L. Highly precise determination of optical constants and sample thickness in terahertz time-domain spectroscopy. *Appl. Opt.* **38**, 409 (1999).
41. Grischkowsky, D., Keiding, S., van Exter, M. & Fattinger, C. Far-infrared time-domain spectroscopy with terahertz beams of dielectrics and semiconductors. *J. Opt. Soc. Am. B* **7**, 2006 (1990).
42. Blundell, S. *Magnetism in condensed matter*. (Oxford University Press, 2001).
43. Yamaguchi, K., Nakajima, M. & Suemoto, T. Coherent control of spin precession motion with impulsive magnetic fields of half-cycle terahertz radiation. *Phys. Rev. Lett.* **105**, (2010).
44. Lee, J. H. *et al.* Spin-canting-induced improper ferroelectricity and spontaneous

- magnetization reversal in SmFeO₃. *Phys. Rev. Lett.* **107**, (2011).
45. Fu, X. J. & Zhou, J. Terahertz magnetic response in ReFeO₃-Type antiferromagnetism. in *Advanced Materials Research* **873**, 757–760 (2014).
 46. Rovillain, P. *et al.* Electric-field control of spin waves at room temperature in multiferroic BiFeO₃. *Nat. Mater.* **9**, 975–979 (2010).
 47. Abdellatif Mohamed, M. A. *Ferrites, Theory and Applications*, 978-3-330-07427-9, 3330074272 ,9783330074279 by Mohamed Abdellatif, Aisha Moustafa. (LAP LAMPERT Academic publishing, 2017).
 48. Nedkov, I. *et al.* Magnetic structure and collective Jahn–Teller distortions in nanostructured particles of CuFe₂O₄. *Appl. Surf. Sci.* **253**, 2589–2596 (2006).
 49. Ferrand, D. *et al.* Applications of II ± VI diluted magnetic semiconductors for magneto-electronics. **119**, 237–244 (2001).
 50. Heck, C. & Heck, C. 1 – Introduction. in *Magnetic Materials and their Applications* 1–3 (1974). doi:10.1016/B978-0-408-70399-4.50004-1
 51. Abdellatif, M. H., Azab, A. A. & Salerno, M. Effect of rare earth doping on the vibrational spectra of spinel Mn-Cr ferrite. *Mater. Res. Bull.* **97**, (2018).
 52. Namai, A. *et al.* Hard magnetic ferrite with a gigantic coercivity and high frequency millimetre wave rotation. *Nat. Commun.* **3**, (2012).
 53. Vinoy, K. J. *Radar absorbing materials : from theory to design and characterization*. (Springer, 2012).
 54. Abdellatif, M. H., Azab, A. A. & Moustafa, A. M. Dielectric Spectroscopy of Localized Electrical Charges in Ferrite Thin Film. *J. Electron. Mater.* **47**, 378–384 (2018).
 55. Ray, A. K. *et al.* Optical absorption in metal bisphthalocyanine sublimed films. *Vacuum* **61**, 19–27 (2001).
 56. Itoh, T. *Ion beam assisted film growth*. (Elsevier, 1989).
 57. Guillén, C. & Herrero, J. Structural, optical and electrical characteristics of ITO thin films deposited by sputtering on different polyester substrates. *Mater. Chem. Phys.* **112**, 641–644 (2008).
 58. Prathap, P., Revathi, N., Reddy, K. T. R. & Miles, R. W. Thickness dependence of structure and optoelectronic properties of In₂O₃:Mo films prepared by spray pyrolysis. *Thin Solid Films* **518**, 1271–1274 (2009).
 59. Furukawa, S. & Miyasato, T. Quantum size effects on the optical band gap of microcrystalline Si:H. *Phys. Rev. B* **38**, 5726–5729 (1988).
 60. Sichert, J. A. *et al.* Quantum Size Effect in Organometal Halide Perovskite Nanoplatelets. *Nano Lett.* **15**, 6521–6527 (2015).
 61. Wang, Y. & Herron, N. Quantum size effects on the exciton energy of CdS clusters. *Phys. Rev. B* **42**, 7253–7255 (1990).
 62. Altieri, P. *et al.* Optical properties of InAs/Al_yGa_{1-y}As/GaAs quantum dot structures. *Mater. Sci. Eng. B* **88**, 234–237 (2002).
 63. Peng, X. *et al.* Shape control of CdSe nanocrystals. *Nature* **404**, 59–61 (2000).
 64. Tauc, J. & Menth, A. States in the gap. *J. Non. Cryst. Solids* **8–10**, 569–585 (1972).
 65. Kavak, H., Eker, S. & Mamedov, A. *Harmonic oscillator model and determination of optical parameters. Journal of Quantitative Spectroscopy and Radiative Transfer* **86**, (2004).
 66. Wemple, S. H. & DiDomenico, M. Behavior of the Electronic Dielectric Constant in Covalent and Ionic Materials. *Phys. Rev. B* **3**, 1338–1351 (1971).
 67. Dötsch, H., Tolsdorf, W. & Welz, F. Domain-wall oscillation of bubble and stripe lattices in hexagonal ferrites. *J. Appl. Phys.* **51**, 3816 (1980).

Authors statement

Conceptualization, Methodology, Investigation, Data curation, Writing - original draft: MHA; Formal analysis: MHA and ME; Funding acquisition, Project administration: PF; Supervision: PF and MS; Resources: PF and ME; Writing - review & editing: MS.

Highlights

- spinel ferrites are useful technologically and as crystal physics model
- zinc ferrite nanoparticles were fabricated by autocombustion
- magneto-optical properties were investigated in THz domain
- coordination number and crystal symmetry determine nanoparticle properties